LETTERS
PUBLISHED ONLINE: 6 JUNE 2016 | DOI: 10.1038/NNANO.2016.85
nature nanotechnology

Coherent commensurate electronic states at the interface between misoriented graphene layers

Elad Koren[1]*, Itai Leven[2], Emanuel Lörtscher[1], Armin Knoll[1], Oded Hod[2] and Urs Duerig[1]*

Graphene and layered materials in general exhibit rich physics and application potential owing to their exceptional electronic properties, which arise from the intricate π-orbital coupling and the symmetry breaking in twisted bilayer systems[1–14]. Here, we report room-temperature experiments to study electrical transport across a bilayer graphene interface with a well-defined rotation angle between the layers that is controllable *in situ*. This twisted interface is artificially created in mesoscopic pillars made of highly oriented pyrolytic graphite by mechanical actuation. The overall measured angular dependence of the conductivity is consistent with a phonon-assisted transport mechanism that preserves the electron momentum of conduction electrons passing the interface[15]. The most intriguing observations are sharp conductivity peaks at interlayer rotation angles of 21.8° and 38.2°. These angles correspond to a commensurate crystalline superstructure leading to a coherent two-dimensional (2D) electronic interface state. Such states, predicted by theory[16,17], form the basis for a new class of 2D weakly coupled bilayer systems with hitherto unexplored properties and applications.

Twisted graphene is characterized by a rotational mismatch between adjacent graphene sheets that results in a Moiré superstructure. In general, the superstructure is incommensurate with the graphite lattice leading to a strong suppression of the interlayer coupling, particularly for rotation angles >10°. As a consequence, the single-layer electronic spectrum reappears for twisted graphene systems[11], a striking phenomenon considering the subnanometre separation between the graphene layers. Owing to the enhanced interlayer coupling at rotation angles <10° the Dirac cones of the single layers open up, which corresponds to a lowering of the Fermi velocity known as renormalization[12–14]. For specific rotation angles such as $30° \pm 8.21°$, $30° \pm 2.20°$ and $30° \pm 16.82°$ (refs 14, 16–18) the superstructure is commensurate with the graphite lattice and forms a strictly periodic interface structure. As a result, the π-orbital coupling across the superlattice unit cells is phase coherent, giving rise to massive Dirac bands at the K points of the Brillouin zone of the superstructure[16,17]. The associated electronic interface states enable efficient interlayer transport at the Fermi energy in a narrow angular range on the order of a few tenths of a degree around the commensurate angles, however, this has never been confirmed experimentally.

Experimentally exploring the transport properties of twisted bilayer systems is extremely challenging as it requires accurate handling, orientation and manipulation of the 2D materials. To this end, we artificially create a planar and well-defined rotational defect in a cylindrical highly oriented pyrolytic graphite (HOPG) mesa structure that acts as a support and manipulator for the bilayer interface. An electrical potential is applied across the mesa and the current flow along the mesa axis is measured, allowing the fundamental electronic coupling mechanisms at the rotated interface to be investigated as a function of the rotation.

Cylindrical HOPG pillars equipped with a lever arm (Fig. 1) were fabricated on a bulk HOPG substrate using previously described methods[19]. The structures used in this work have identical dimensions: the radius of the cylindrical section is 330 nm and the pillar height is 50 nm. The lever arm that is used for the rotation actuation has a length and width of 1 μm and 200 nm, respectively. These structures were found to work best in the experiments. We experienced difficulties with stabilizing the rotation axis in pillars with smaller radii whereas larger structures could not be reliably sheared at a single glide plane (Supplementary Information Section 2). The structures are covered with a Pd/Au metal layer (15 and 30 nm thick, respectively), which serves as an electrical top contact. Conductance measurements were performed at room temperature and under ambient conditions using an atomic force microscope (AFM) and electrically conducting Pt/Ir coated tips. We apply a torque force to the mesa structure by pushing horizontally against the lever arm from the side with the AFM tip. This mechanical actuation results in the spontaneous formation of a single rotational planar defect within the HOPG mesa. At the same time a good electrical contact between the tip and the top metal electrode is formed. The rotation angle θ is controlled by moving the AFM tip on a circular trajectory with ~0.1° precision (Fig. 1). Despite the non-centric actuation, the rotation axis remains located at the centre of the pillar due to stabilizing adhesive line tension forces[19].

The conductance is measured by monitoring the current flow through the HOPG structure at a fixed bias potential while continuously rotating the lever arm in one rotation direction, either clockwise or anticlockwise. A current profile can only be recorded once for a particular pillar structure as explained in Section 2 of the Supplementary Information. Therefore, each data set shown here corresponds to an independent measurement performed on a different pillar sample. Figure 2a shows three examples of current data recorded over an angular range of 60° and at a bias potential of 50 mV. Such curves are routinely observed in approximately 90% of the cases. The reflection symmetry of the data with respect to 30° is consistent with the lattice symmetry and thus strongly supports the single glide plane sliding mechanism. In contrast, unsuccessful experiments are characterized by abrupt discontinuities in the recorded current traces and the lack of reflection symmetry.

The interface conductivity $\sigma_{int}(\theta)$ (Fig. 2b) is derived by assuming constant values for the resistance of the tip–sample contact during rotation, which is dominated by the cantilever resistance, $270 \pm 10\ \Omega$ (ref. 20), and the mesa sections above and below the twisted interface. The latter is on the order of $460 \pm 30\ \Omega$, which is consistent with the expected value of the *c* axis resistivity of

[1]IBM Research - Zurich, Rueschlikon 8803, Switzerland. [2]Department of Physical Chemistry, School of Chemistry, The Raymond and Beverly Sackler Faculty of Exact Sciences and The Sackler Center for Computational Molecular and Materials Science, Tel Aviv University, Tel Aviv 6997801, Israel.
*e-mail: elk@zurich.ibm.com; drg@zurich.ibm.com

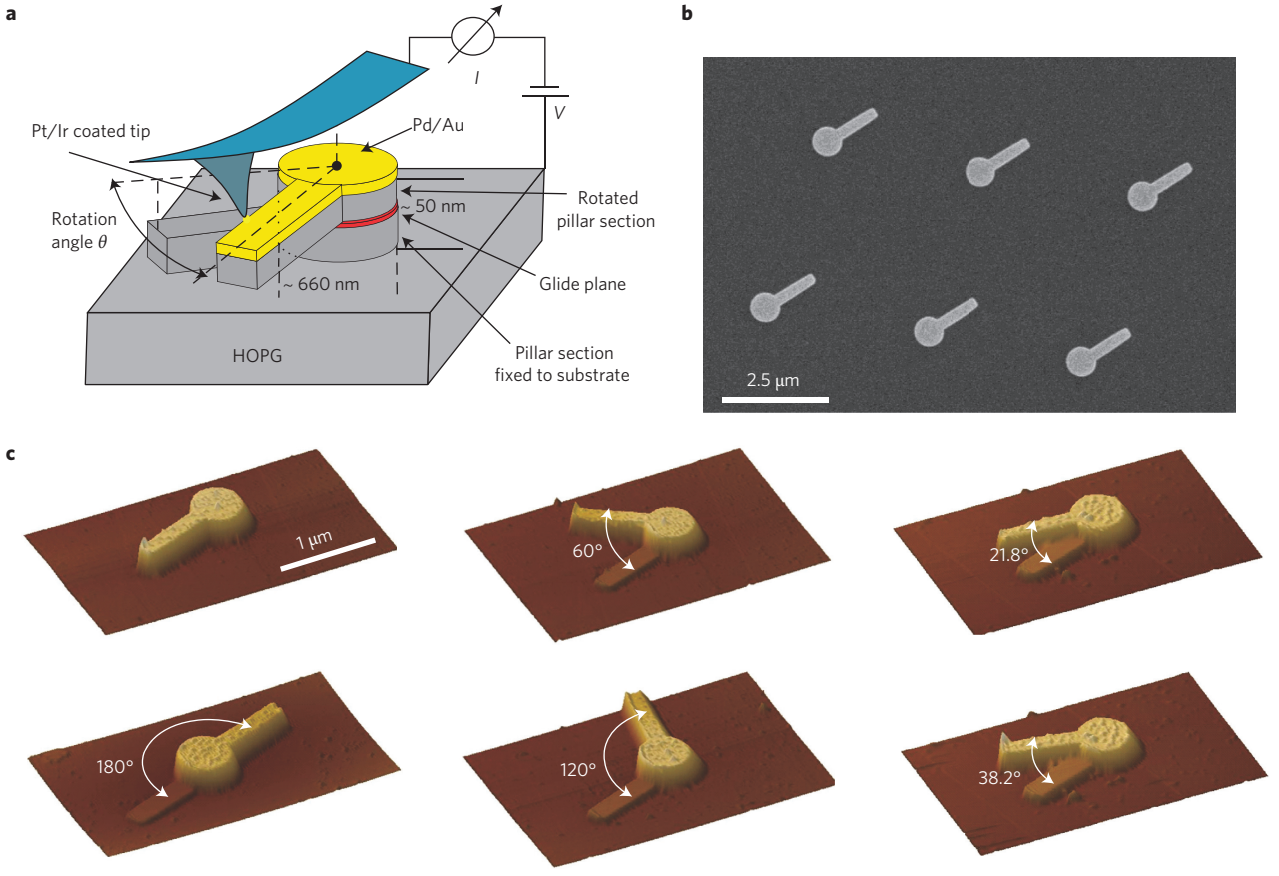

Figure 1 | Experimental procedure. a, Schematic of the AFM experiment used to create a twisted interface within an HOPG mesa structure and to control the rotation angle. The mesa structures are approximately 50 nm tall. The circular section has a diameter of 660 nm and the leaver arm is 200 nm wide and 1 μm long. A bias potential V is applied to the top Pd/Au metal electrode using a conducting AFM cantilever, whereas the bulk graphite sample is at ground potential. **b**, Scanning electron microscopy image of fabricated mesas. **c**, AFM images showing stable rotational configurations both before and after the mechanical actuation at angular positions of 0°, 60°, 120° and 180°. The sixfold symmetry of the graphite lattice imposes a stronger binding for the above configurations. The structure can also be arrested at any arbitrary intermediate rotation angle as shown for $\theta = 21.8°$ and 38.2°.

3.8×10^{-3} Ωm measured previously in such structures[20]. Furthermore we normalize the interface conductivity plateaus observed close to a 0° rotation angle to the interface conductivity of a single stacking fault defect given by 0.6 S μm^{-2} × $A \sim 0.02$ S where $A = \pi r^2 \approx 0.34$ μm^2 is the cross-sectional area of the pillar[20] (for more details see Methods and Supplementary Information Section 3).

Surprisingly, the conductivity decreases gradually even at large rotation angles, that is $\theta > 10°$, although the current transport was theoretically predicted to be substantially suppressed in this regime on the basis of tunnelling transport calculations[18]. A smooth angular dependence and enhanced interlayer conductivity has recently been predicted[15], suggesting that the momentum mismatch between the electronic states of the twisted layers can be overcome by incoherent scattering from the lattice vibrations of the beating mode branch. A temperature dependent interlayer conductivity was recently observed[21] in twisted bilayer graphene, in support of a phonon assisted transport channel. The interlayer conductivity due to phonon scattering is given by[15]:

$$\sigma_{\mathrm{ph}}(\theta) \propto \frac{n_\theta}{\omega_\theta} \frac{E_{\mathrm{F}}^2}{v_{\mathrm{F}}^4}$$

where n_θ is the thermal population of the beating phonon mode of frequency ω_θ at wave vector q_θ that connects the rotated Dirac points and v_{F} is the Fermi velocity in graphene (Supplementary Information Section 3). With n_θ and ω_θ given by well-established relations, the Fermi energy E_{F} remains the only free fit parameter.

An excellent fit to the angular dependence of the measured data is obtained for $10° < \theta < 50°$ yielding $E_{\mathrm{F}} = 0.12$ eV with a fit uncertainty of ±0.02 eV (solid blue line in Fig. 2b). To account for the rapid increase in the interlayer conductivity at small angular mismatch configurations with respect to the high symmetry points at integer multiples of 60°, renormalization—which leads to a pronounced enhancement of the scattering efficiency and thus the conductivity—must be accounted for. The effect is parameterized in terms of a transverse hopping integral for which we obtain a value of $t_\perp = 0.18$ eV with a fit uncertainty of ±0.05 eV (solid red line in Fig. 2b). The fit parameters are reproducible among different samples and virtually independent from the applied bias voltage. As mean values we find $E_{\mathrm{F}} = 0.12$ eV and $t_\perp = 0.2$ eV with a sample dependent variance of 0.01 eV in both cases (Supplementary Information Section 4).

The phonon-assisted transport model provides a good quantitative description of the angle dependent interface conductivity but the minimum interface conductivity measured at 30° is consistently higher than the predicted value. This shift, termed the offset conductivity σ_{offset}, is clearly dependent on the applied bias V and we attribute this deviation to a competing parallel tunnelling conduction. Specifically we find $\sigma_{\mathrm{offset}} = 1.7 \pm 0.15$ mS μm^{-2} and 2.65 ± 0.1 mS μm^{-2} at $V = 0.05$ V and 0.25 V, respectively, increasing to ~10 mS μm^{-2} at $V = 3$ V. Note, however, that the effective interface potential is substantially less than V, by a factor of ~2 for $V < 0.25$ V rising to a factor of ~7 for $V = 3$ V due to the series resistances in the system (Supplementary Information Section 4).

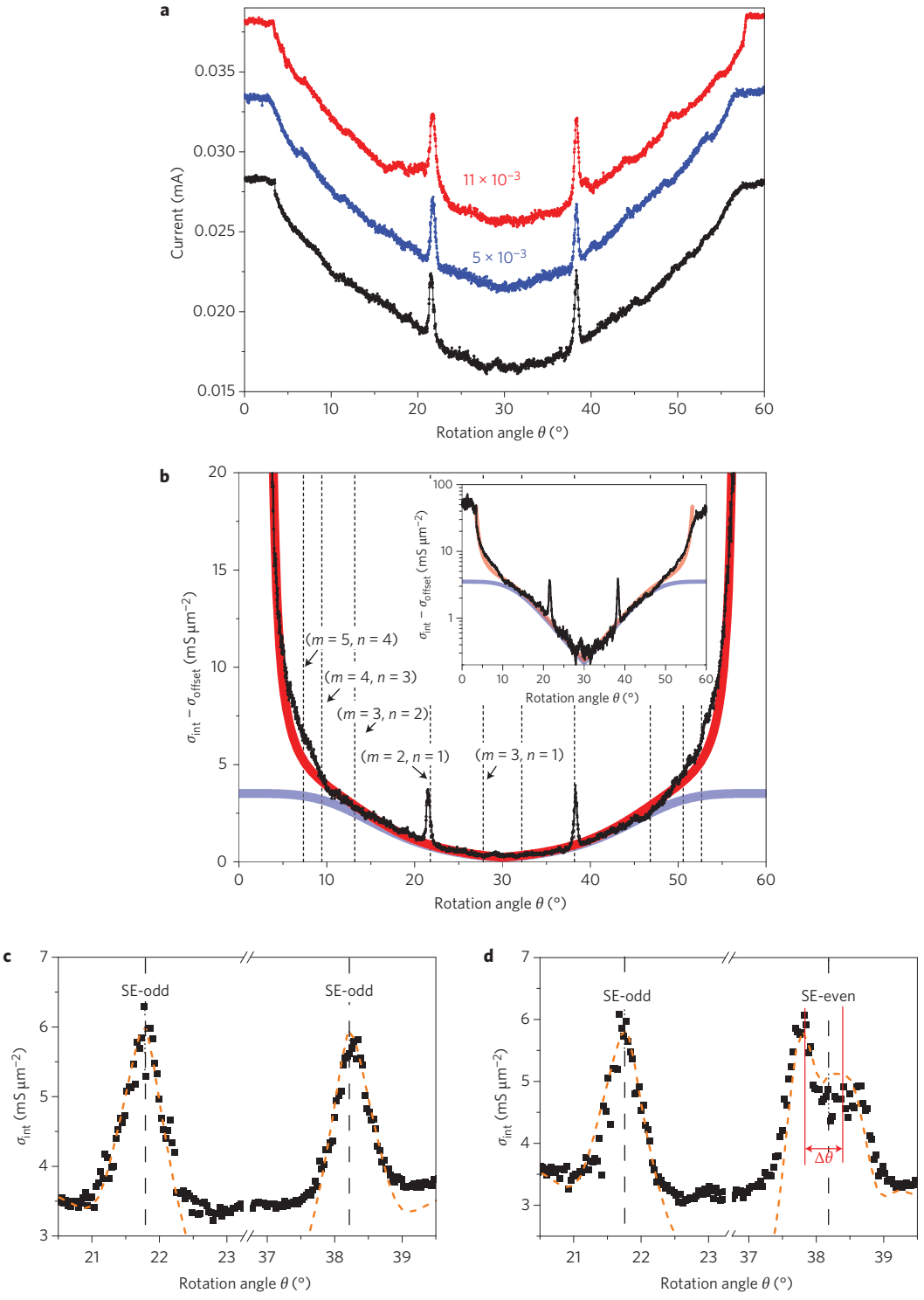

Figure 2 | Interlayer conductivity. a, Measured current flowing through the HOPG structure at a bias potential of $V = 50$ mV while continuously rotating the lever arm. Three independent data samples obtained from different pillar structures are shown. Blue and red traces are offset by 5 and 11 μA, respectively. **b**, Interface conductivity minus a constant offset $\sigma_{offset} = 1.9$ mS μm^{-2} derived from the measured current (black curve in **a**) and calculated interlayer conductivity due to phonon scattering neglecting (blue line) and including (red line) the effect of Fermi velocity renormalization. The vertical dashed lines represent the positions of commensurate twisted configurations with $\theta = 7.34°$, 9.43°, 13.2°, 21.8° and 27.8°. Inset: Semilogarithmic plot of the same data. **c**,**d**, Conductivity profiles measured at $V = 0.25$ V (black curves) in the vicinity of the commensurate configurations at 21.8° and 38.2°. The peak positions, structure and amplitudes are reproduced with excellent agreement by a tight-binding calculation (dashed orange line, vertically shifted by −9.3 mS μm^{-2}) considering a hexagonal flake with a side length of 8.2 nm and using a bias voltage of 0.1 V in accordance with the effective voltage drop at the twisted interface in the measured devices. **c**, A rotation around a hexagon centred (Supplementary Fig. 12a) axis yields a SE-odd (Bernal) stacked twisted graphene bilayer for $\theta = 21.8°$ and 38.2° with a single conductivity peak centred at the commensurate angles. **d**, For a rotation around an atom-centred axis (Supplementary Fig. 12a), the twisted graphene bilayer assumes a SE-odd stacking symmetry for $\theta = 21.8°$ (single peak) whereas for $\theta = 38.2°$ the stacking symmetry is SE-even (hexagonal AA) resulting in a double peak structure split by an angle $\Delta\theta \approx 0.5°$.

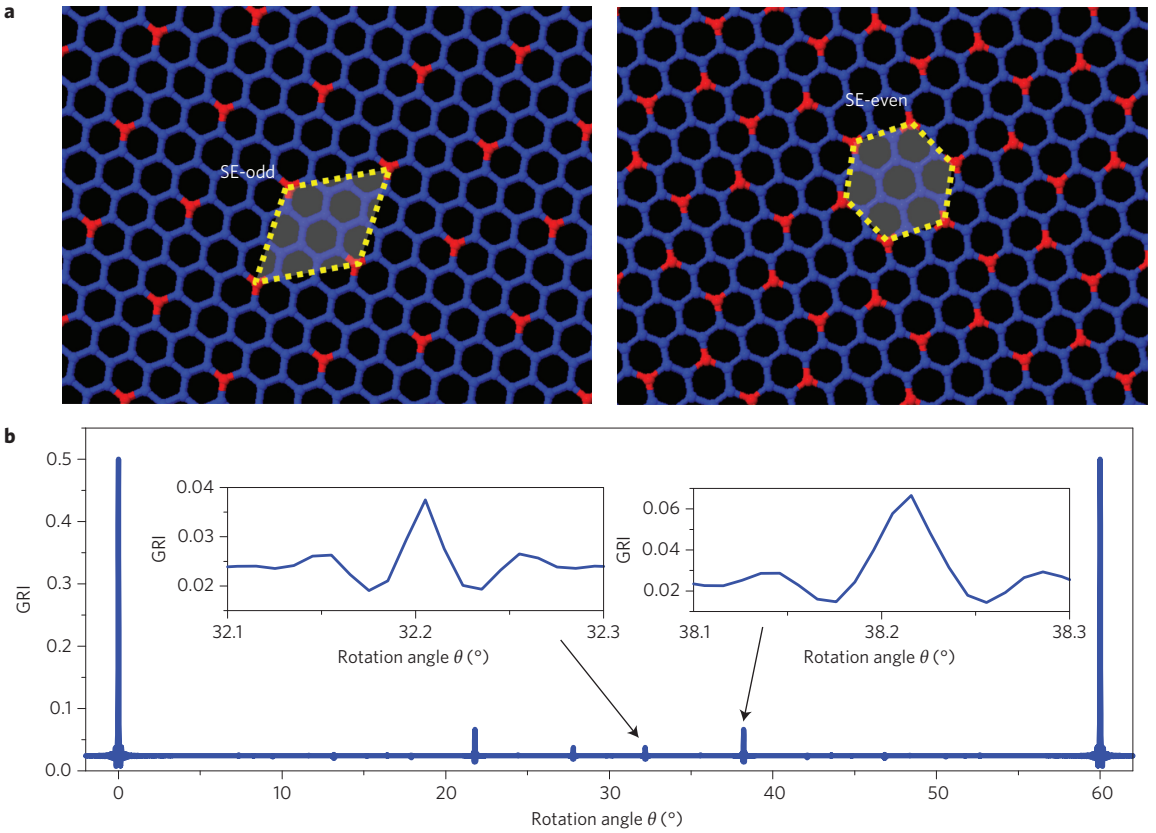

Figure 3 | Commensurate twisted configurations. a, Local registry index (LRI) maps for $\theta = 21.8°$ and 38.2° showing the degree of atomic overlap for SE-odd symmetry (left), corresponding to Bernal like stacking with the A atoms of the top layer overlapping with B atoms of the bottom layer at the corner points of the superlattice unit cell, and SE-even symmetry (right), corresponding to a hexagonal AA-like stacking. Fully eclipsed interlayer atomic positions are colour coded in red whereas non-overlapping atomic positions are dark blue. **b**, The GRI as function of θ, obtained by rotating a 100 nm diameter circular bilayer flake around a hexagon-centred axis starting from a Bernal stacking configuration at $\theta = 0°$.

The most intriguing features of the conductivity profiles are the sharp peaks that emerge at interlayer misfit angles of 21.8° and 38.2°, corresponding exactly to commensurate twisted stacking configurations. These peaks, with an amplitude of 3.7 ± 0.5 mS μm^{-2} with respect to the offset conductivity, are reproduced in all samples. The peak amplitude is virtually independent of the applied bias up to $V \sim 1$ V, whereas for $V > 2$ V the peaks are masked by the offset conductivity (Supplementary Information Section 4). Pronounced conductivity peaks have been theoretically predicted[18] for a series of commensurate angles $\theta = (30 \pm 8.2)°$, $(30 \pm 2.2)°$ and $(30 \pm 16.8)°$, where the first two angles perfectly agree with our observations within the experimental resolution. Commensurate superstructures are strictly periodic as the corresponding superlattice vectors $\mathbf{L}_{\mathrm{SL}\,1,2}(\theta_{m,n}) = m\,\mathbf{a}_{1,2} + n\,\mathbf{a}_{2,1}$ can be written in terms of an integer sum of the lattice vectors $\mathbf{a}_{1,2} = a(\pm(1/2)\mathbf{e}_x + (\sqrt{3}/2)\mathbf{e}_y)$ of the graphene sheets where $a = 0.246$ nm. The observed peaks appear at the lowest index commensurate angles $\theta_{m,n}$ with $m = 2$ and $n = 1$, which also have the smallest superlattice parameter, $L_{\mathrm{SL}} = 0.651$ nm, of all of the possible commensurate twisted structures.

Commensurate twisted bilayer graphene can be realized in two distinct configurations as shown in the local registry index (LRI) map (Fig. 3a), which provides a real-space visualization of the local interlayer atomic overlap (Supplementary Information Section 8). The configurations are characterized by SE-odd and SE-even sublattice exchange symmetry[17]. The SE-odd structure resembles Bernal stacking, where A sites at the edges of the primitive supercell in one layer reside atop corresponding B sites in the adjacent layer. The SE-even structure is characterized by a hexagonal superlattice with AA stacking of the primitive supercell. We note that both SE-odd and SE-even configurations can be realized for each of the commensuration angles and the transition between the two involves a very small lateral (in-plane) displacement (typically < 1 Å) of one of the graphene layers with respect to the other.

As a rule, the measured conductance peaks are triangular in shape and centred at the commensurate angles (Fig. 2c). In a few rare cases—approximately 5–10% of the experiments—we also observed double-peak structures with the peak positions offset by ~0.5°. These double peaks occur either at 21.8° or 38.2° (Supplementary Information Section 5). An example with a single peak at 21.8° and a double peak at 38.2° is shown in Fig. 2d. The angular positions and the peak profiles are perfectly reproduced within experimental resolution by numerical calculations (dashed orange lines in Fig. 2c,d) based on the Landauer[22] formalism and a tight-binding model that includes intralayer nearest neighbours interactions and distance-dependent interlayer hopping integrals[15,23]. The calculations were performed for a hexagonally shaped twisted bilayer graphene system with an outer radius of 8.2 nm and the bilayer was embedded between virtual metallic electrodes that mimic the HOPG substrate (Supplementary Information Section 7). From the numerical results we can also unambiguously assign the single- and double-peak structures to SE-odd and SE-even sublattice exchange symmetry, respectively.

Turning to a momentum space description, the conductivity enhancement and the peak fine structure for commensurate twisted configurations can be rationalized in terms of a crystal momentum exchange with the superstructure that connects $\mathrm{K}_{\mathrm{top}}$ points of the top graphene sheet with the respective $\mathrm{K}_{\mathrm{bottom}}$ points of the lower sheet (Fig. 4a). This Umklapp scattering process enables

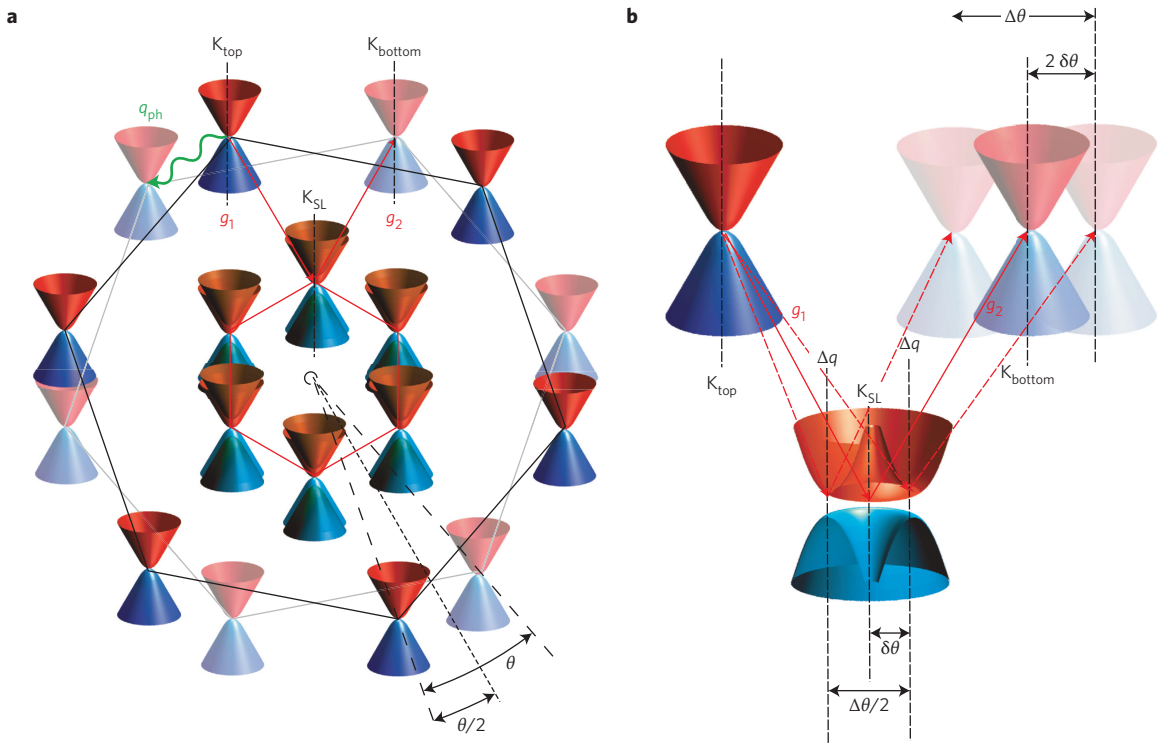

Figure 4 | Momentum-space representation of bilayer graphene coupling at commensurate twist angles θ = 21.8° and 38.2°. a, Electronic states corresponding to massive Dirac cones (not to scale) at the K_{top} and K_{bottom} points of the Brillouin zone of the top (black hexagon) and bottom (light gray hexagon) graphene sheets are coupled via an Umklapp scattering process involving a lattice momentum exchange indicated by the reciprocal superlattice vectors g_1 and g_2. The superlattice Brillouin zone (red hexagon) is rotated by $\theta/2 + 30°$ with respect to the top sheet. The coupling gives rise to a 2D electronic interface state that may have different sublattice exchange (SE) symmetry. For SE-odd stacking symmetry two gapped and two touching massive Dirac bands (not to scale) centred at the K_{SL} points of the Brillouin zone are formed. The competing coupling mechanism that bridges the momentum mismatch between K_{top} and K_{bottom} via a phonon momentum exchange g_{ph} is indicated by the green arrow. Note that phonon coupling is also active for non-commensurate superstructures with arbitrary twist angle θ. **b**, For SE-even stacking symmetry, the massive Dirac bands (not to scale) are slightly gapped (~10–20 meV) and shifted by $\Delta q \sim \pm 0.01\,nm^{-1}$ with rotational symmetry with respect to the K_{SL} points. Optimal coupling is obtained by rotating the reciprocal superlattice by a small angle $\delta\theta$ such that the K_{top} and K_{bottom} points are connected to the respective conduction band minima by equal magnitude momentum vectors (red dashed lines) resulting in a double-peak structure of the transverse conductivity with an angular peak separation $\Delta\theta$.

momentum-conserving coupling between electrons at E_F in the two layers. The resulting eigenstates for SE-odd symmetry form two gapped (~40 meV) and two touching massive Dirac bands centred at the K_{SL} points of the Brillouin zone of the superlattice[17]. Consistent with this band structure, we find one single triangular conductivity peak exactly at the commensuration angle. For SE-even symmetry, the massive Dirac bands are slightly gapped (~10–20 meV) and shifted by $\Delta q \sim \pm 0.01\ nm^{-1}$ with rotational symmetry with respect to the K_{SL} points (Fig. 4b). We expect to observe conductivity maxima when the K_{top} and K_{bottom} points are connected with the conduction band minima of the superstructure by equal magnitude momentum vectors (Fig. 4b), yielding minimal mismatch between the exchanged and crystal momenta of the superstructure. This condition is fulfilled if the reciprocal superlattice is rotated by a small angle $\delta\theta \approx \Delta q/K_{SL}$ that corresponds to a further rotation of the graphene sheets by $2\delta\theta$. Therefore, the peak splitting $\Delta\theta$ can be expressed in terms of a momentum condition $\pm\Delta q \cong K_{SL}\Delta\theta/4$ with $K_{SL} = 4\pi/3L_{SL}$. From the experimentally observed $\Delta\theta \sim 0.5°$ we obtain $\Delta q \sim \pm 0.014\ nm^{-1}$, in good agreement with the band structure calculation[17] considering the experimental uncertainties.

An infinite number of commensurate configurations exist at $\theta_{mn} = \cos^{-1}((6mn + (m-n)^2)/(6mn + 2(m-n)^2))$, where $m > n$ are integers. The corresponding supperlattice constants are equal to the Moiré period $L_M = a/\sqrt{(2 - 2\cos\theta)}$ for angles $\theta_{m,n}$ with $n = m - 1$ and greater than L_M in all other cases. One may wonder why no evidence for a conductance enhancement appears at commensurate angles other than $\theta = 21.8°$ and 38.2°. To explain this we note that the interlayer transport is related to the degree of overlap between the p_z orbitals of the carbon atoms in adjacent layers, which can be quantified in terms of a global registry index (GRI). The latter is defined as the sum of the LRI normalized by the corresponding sums for Bernal (AB) and hexagonal AA stacked bilayer graphene (Fig. 3b). Sharp GRI peaks appear at the commensurate twist angles whereby the largest peak value of $\Delta GRI \approx 0.042$ is obtained for $\theta = 21.8°$ and 38.2°. However, we do not find experimental evidence for the commensurate states at 27.8° and 32.2° with $\Delta GRI \approx 0.013$ whereas naively one would expect the peak height to scale with ΔGRI ratio (Supplementary Fig. 12). This implies that the interlayer orbital coupling is a delicate process involving Bloch phase cancellations. In fact, our tight-binding calculations (Supplementary Fig. 10) as well as theoretical works[18,23] predict a peak ratio of <0.1 and the signature of the state is likely to be masked by the offset conductivity and the phonon-assisted transport contribution in our room-temperature experiment. A much richer peak structure, particularly for commensurate angles with $n = m - 1$, may emerge by freezing out the phonon scattering at low temperature. Finally, the reported electronic characteristics are of a general nature and apply for other weakly coupled layered systems, such as hexagonal BN, MoS_2 or WS_2. The mechanical realization of commensurate configurations also seems to have significant practical value, as it provides a means for generating artificial 2D electronic states that can be turned on and off by minute angular displacements.

Methods

Methods and any associated references are available in the online version of the paper.

Received 2 October 2015; accepted 26 April 2016; published online 6 June 2016

References

1. Geim, A. K. Graphene: status and prospects. *Science* **324,** 1530–1534 (2009).
2. Ponomarenko, L. A. *et al.* Cloning of dirac fermions in graphene superlattices. *Nature* **497,** 594–597 (2013).
3. Yankowitz, M. *et al.* Emergence of superlattice Dirac points in graphene on hexagonal boron nitride. *Nature Phys.* **8,** 382–386 (2012).
4. Dean, C. R. *et al.* Hofstadter's butterfly and the fractal quantum hall effect in moiré superlattices. *Nature* **497,** 598–602 (2013).
5. Hunt, B. *et al.* Massive Dirac fermions and Hofstadter butterfly in a van der Waals heterostructure. *Science* **340,** 1427–1430 (2013).
6. Schmidt, H., Rode, J. C., Smirnov, D. & Haug, R. J. Superlattice structures in twisted bilayers of folded graphene. *Nature Commun.* **5,** 5742 (2014).
7. Li, G. *et al.* Observation of Van Hove singularities in twisted graphene layers. *Nature Phys.* **6,** 109–113 (2009).
8. Kim, K. S. *et al.* Coexisting massive and massless Dirac fermions in symmetry-broken bilayer graphene. *Nature Mater.* **12,** 887–892 (2013).
9. Trambly de Laissardière, G., Mayou, D. & Magaud, L. Localization of Dirac electrons in rotated graphene bilayers. *Nano Lett.* **10,** 804–808 (2010).
10. Lee, D. S. *et al.* Quantum hall effect in twisted bilayer graphene. *Phys. Rev. Lett.* **107,** 216602 (2011).
11. Hass, J. *et al.* Why multilayer graphene on 4 H – SiC $(000\bar{1})$ behaves like a single sheet of graphene. *Phys. Rev. Lett.* **100,** 125504 (2008).
12. Luican, A. *et al.* Single-layer behavior and its breakdown in twisted graphene layers. *Phys. Rev. Lett.* **106,** 126802 (2011).
13. Lopes dos Santos, J. M. B., Peres, N. M. R. & Castro Neto, A. H. Graphene bilayer with a twist: electronic structure. *Phys. Rev. Lett.* **99,** 256802 (2007).
14. Shallcross, S., Sharma, S., Kandelaki, E. & Pankratov, O. A. Electronic structure of turbostratic graphene. *Phys. Rev. B* **81,** 165105 (2010).
15. Perebeinos, V., Tersoff, J. & Avouris, P. Phonon-mediated interlayer conductance in twisted graphene bilayers. *Phys. Rev. Lett.* **109,** 236604 (2012).
16. Shallcross, S., Sharma, S. & Pankratov, O. A. Quantum interference at the twist boundary in graphene. *Phys. Rev. Lett.* **101,** 056803 (2008).
17. Mele, E. J. Commensuration and interlayer coherence in twisted bilayer graphene. *Phys. Rev. B* **81,** 161405 (2010).
18. Bistritzer, R. & MacDonald, A. H. Transport between twisted graphene layers. *Phys. Rev. B* **81,** 245412 (2010).
19. Koren, E., Lörtscher, E., Rawlings, C., Knoll, A. W. & Duerig, U. Adhesion and friction in mesoscopic graphite contacts. *Science* **348,** 679–683 (2015).
20. Koren, E., Knoll, A. W., Lörtscher, E. & Duerig, U. Direct experimental observation of stacking fault scattering in highly oriented pyrolytic graphite meso-structures. *Nature Commun.* **5,** 5837 (2014).
21. Kim, Y. *et al.* Breakdown of the interlayer coherence in twisted bilayer graphene. *Phys. Rev. Lett.* **110,** 096602 (2013).
22. Datta, S. *Quantum Transport: Atom to Transistor* (Cambridge Univ. Press, 2005).
23. Habib, K. M. M., Sylvia, S. S., Ge, S., Neupane, M. & Lake, R. K. The coherent interlayer resistance of a single, rotated interface between two stacks of AB graphite. *Appl. Phys. Lett.* **103,** 243114 (2013).

Acknowledgements

We thank U. Drechsler and M. Tschudy for invaluable technical support and J. Tersoff, V. Perebeinos, N. Moll and R. Allenspach for stimulating discussions. The work was supported by the FP7 Marie Curie Actions of the European Commission, ITN fellowship cQOM (Project ID 290161) and by the Swiss National Science Foundation, Ambizione Grant No. PZ00P2 161388 (E.K.). Work at TAU was supported by the Israel Science Foundation under grant No. 1740/13, the Lise-Meitner Minerva Center for Computational Quantum Chemistry, and the Center for Nanoscience and Nanotechnology at Tel-Aviv University.

Author contributions

E.K., A.K. and U.D. jointly conceived the experimental concept. E.K. performed the experimental work including reactive ion etching, AFM characterization, electrical transport measurements and data analysis. E.K. also participated in the writing of the manuscript. A.K. provided operational guidance for the AFM. E.L. was responsible for the electron beam lithography and metal lift-off process for the fabrication of the metal masks. U.D. was responsible for the writing of the manuscript. I.L. participated in the development of the global (GRI) and local (LRI) registry index concept and implemented them within a computational code. I.L. also performed the numerical calculations of the GRI, LRI and interlayer transport and participated in the writing of the manuscript. O.H. conceived the concept of the GRI and LRI, developed and implemented the interlayer transport code and participated in the writing of the manuscript.

Additional information

Supplementary information is available in the online version of the paper. Reprints and permissions information is available online at www.nature.com/reprints. Correspondence and requests for materials should be addressed to E.K. and U.D.

Competing financial interests

The authors declare no competing financial interests.

Methods

Sample preparation. High-quality HOPG (μ–mash, ZYA grade, 0.4° mosaic spread) centimetre-size samples with a thickness of approximately 2 mm were used as substrates. The graphite structures were fabricated from a freshly cleaved HOPG substrate by means of anisotropic oxygen plasma etching. In the first step Pd/Au metal masks were deposited onto the HOPG surface. The metal masks were fabricated by means of electron beam lithography and lift-off using a 100 nm thick poly-methyl-methacrylate (MICRO CHEM 950 PMMA) resist layer. The metal masks consist of 15 nm of Pd as an adhesion promoter to the HOPG surface and 30 nm of Au as the top layer; the metal layers were deposited by means of thermal evaporation. Before evaporation, short-duration oxygen plasma cleaning was applied to remove resist residues on the exposed HOPG surface. The mesa structures with a height of ~50 nm emerges during the plasma etch, which selectively thins down only the unprotected HOPG area (Fig. 1b). Reactive ion etching was performed using an Oxford Plasma Lab 80 plus tool. An oxygen pressure of 20 mbar and bias potential of 200 V were optimized to obtain a low etch rate of 11 nm min^{-1} for good control of the mesa height and to minimize chemical anisotropic side-wall etching.

Rotation manipulation. The experiments were conducted at ambient conditions using a commercial AFM (Bruker Dimension V) and Pt/Ir coated AFM probes (SCM-PIT, Bruker Ltd, nominal spring constant 2.8 N m^{-1}). The fabricated mesa structures can be readily imaged in the tapping mode and selected for the experiment. Initially, the tip is placed at an off-centre position touching the lever arm. The tip is then moved at angular velocity of 12° s^{-1} on a circular track with radius $r_{tip} \approx 1$ μm around the centre position of the mesa using the Nanoman manipulation software. As a result of this actuation a tangential tip force builds up, giving rise to a torque $M = F_{tip} r_{tip}$ and a lateral shear force F_{tip} acting at the centre position (Supplementary Figs 1 and 2). As shown in ref. 19 a glide plane defect is spontaneously created within the mesa if the shear force exceeds a threshold of $F_{tip} > 2\sigma r \approx 150$ nN where $\sigma = 0.227$ Nm^{-1} is the interface tension between two graphene sheets and $r = 330$ nm is the radius of the cylindrical mesa section. The top mesa section is essentially free to rotate around the centre axis and to glide along the direction of the applied force as soon as the glide plane defect has been created. The translational glide motion is, however, inhibited by counterbalancing adhesive line tension forces[19] that stabilize the rotation axis at the centre position.

Interface conductivity measurement. The current flow through the pillar (Supplementary Fig. 4) is measured by means of a commercial virtual ground type current–voltage converter (FEMTO DHPCA-100) that is connected to the sample stage via a series resistor of $R_{CL} = 1$ kΩ to limit the maximum current to ~1 mA and via a passive second-order low-pass filter with a cut-off frequency of 100 kHz to avoid overloading of the converter by high-frequency noise signals. The overall measured electrical resistance $R_T(\theta) = R_{CL} + R_P + R_{t-s} + R_{int}(\theta)$ for a given angular configuration θ is composed of the serial elements R_{CL}, R_P, R_{t-s} and $R_{int}(\theta)$. R_P denotes the c axis resistance of the graphite pillar, which is composed of the rotated top and fixed bottom section, R_{t-s} denotes the tip–sample contact resistance and $R_{int}(\theta)$ denotes the resistance of the twisted interface (Supplementary Fig. 4b). We assume that R_P and R_{t-s} are constant throughout the rotation and we obtain for the interface resistance $R_{int}(\theta) = R_T(\theta) - R_P - R_{t-s} - R_{CL}$. However, the large observed scatter of the c axis resistance values in mesoscale graphite samples[20] relative to the low resistance of $R_{int}(\theta = 0)$ yields considerable unknown systematic errors for $R_{int}(\theta)$. Therefore we fix the interface resistance at $\theta = 0°$ to the value of the interface resistance of a stacking fault defect, $R_{int}(\theta = 0) = \rho_{sf}/\pi r^2 \cong 50\Omega$ where $\rho_{sf} \cong 1.7 \times 10^7 \Omega$ nm^{-2} is the specific stacking fault resistivity[20]. This allows us to extract the twisted interface resistance for the entire angular range using $R_{int}(\theta) = R_T(\theta) - (R_T(\theta = 0) - 50\Omega)$ from which the interface conductivity is derived according to $\sigma_{int}(\theta) = (R_{int}(\theta) \times \pi r^2)^{-1}$. We note that our analysis method cannot account accurately for the absolute interface resistance for 0°, but it rather represents an upper limiting value. If we were to estimate the interface resistance from the c axis resistivity $\rho_c \approx 4 \times 10^{-3} \Omega$m we would obtain $R_{int}(\theta = 0) = \rho_c d/\pi r^2 \approx 4\Omega$ where $d = 0.34$ nm is the distance between graphite layers. Importantly, the choice of the value of the interface resistance at $\theta = 0°$ has only a minor effect on the conductivity profile for angular configurations > 5° (Supplementary Fig. 5).